



X-ray tomography image-based reconstruction of microstructural finite element mesh models for heterogeneous materials

Ming Huang, Yue-ming Li*

State Key Laboratory for Strength and Vibration of Mechanical Structures, Xi'an Jiaotong University, 710049 Xi'an, PR China

ARTICLE INFO

Article history:

Received 19 May 2012

Received in revised form 31 July 2012

Accepted 6 August 2012

Available online 29 September 2012

Keywords:

Heterogeneous material

X-ray tomography

Microstructure

Reconstruction

FE mesh model

Material component segmentation

ABSTRACT

This paper presents a method for automatic reconstruction of finite element (FE) mesh models for heterogeneous materials by taking into account their real microstructures. The method is developed by mapping the FE mesh model with the serial images captured by X-ray tomography. The material components are segmented by grayscale thresholds to reflect the microstructures. Improved reconstruction accuracy is achieved by applying the contrast limited adaptive histogram equalization, median filter and pixel interpolation to the serial images. Image trim and pixel merging are proposed to reduce the elements contained in the model. In the reconstruction of $\text{Al}_2\text{O}_3/(\text{W,Ti})\text{C}$ ceramic composite, it is demonstrated that the reconstructed models accurately reflect the microstructural features. By predicting the macroscopic properties numerically based on homogenization method, the reconstructed models are proved to be valid and applicable to FE analysis.

© 2012 Elsevier B.V. All rights reserved.

1. Introduction

Heterogeneous materials that are composed of domains of multiple material components (or phases) are prevalent in natural and synthetic products [1]. Examples include composites, cellular solids, phase-separated metallic alloys and so forth. The macroscopic properties, such as stiffness, strength and toughness, of these materials are determined by their microstructures. Therefore, a thorough understanding of how a heterogeneous material's microstructure affects its macroscopic properties is of great importance in design and development of high performance heterogeneous materials. Various theoretical and numerical methods are proposed to clarify the relationship of the microstructure and the macroscopic property, of which the FE analysis is an important effective method. The FE analysis primarily requires the development of methods to automatically generate geometrical or mesh models to actually take into account complex microstructures of heterogeneous materials. However, due to the very irregular shape and complex distribution of phases, the incorporation of the information about microstructures into the models is one of the challenges in computational mechanics [2].

Numerous methods are developed to overcome the difficulties for modeling. The unit cell models [3] with idealized or disordered shapes and arrangements of material components have a longest history and are most widely used to analyze the microstructure–

macroscopic property relationship. These models, which assume that sufficiently large samples of heterogeneous materials behave homogeneously though the real microstructures are locally heterogeneous [4], are designed in a minimum volume to represent and describe the overall material structure of interest. The unit cell models have been developed from the simplest 2D versions, which assume rather specific shape and distribution of phases, to complex 3D models, which take into account most characteristics of the real shape and distribution of material components [5]. These models appear to be very efficient in the analysis of the effect of constituent, volume fraction, shape and arrangement of phases on the macroscopic properties of the heterogeneous materials. However, evidently unrealistic material structure assumptions are made in these models and the effect of many real microstructures on macroscopic properties are neglected in the analysis using FE techniques [3]. It follows that an accurate simulation of heterogeneous materials can be really obtained only by incorporating actual microstructures into the numerical models.

With the increasing power of digital image processing technologies, new geometrical approaches to model microstructures of heterogeneous materials are emerged. The digital images, which show the realistic internal microstructure of materials, are obtained by detecting the attenuation of beams that penetrate the material (e.g. X-ray tomography) or by photographing the sample from a series of parallel sections (e.g. serial sectioning) [6]. The geometrical surface or solid models are reconstructed by segmenting the digital images into different components and then extracting the edges of the components [7–10] or by using various

* Corresponding author. Tel.: +86 29 82668340; fax: +86 29 82669044.

E-mail address: liyueming@mail.xjtu.edu.cn (Y.-m. Li).

statistical correlation functions that are ascertained from the digital images to quantify the shape and distribution of phases [11–13]. These models considering the inherent morphology, clustering and arrangement of phases, with minimal microstructural approximations, are frequently adopted to analyze the macroscopic behaviors of heterogeneous materials.

Although recent advances have been made in reconstructing the geometrical microstructures of heterogeneous materials, novel methods for generating numerical models are still needed as: (1) current geometrical models should be additionally meshed to perform FE analysis and the elements meshed on the complex geometrical surface and solid are generally in the form of triangular and tetrahedral, which are of low precision for FE analysis; (2) relatively small microstructural features are easily lost during the meshing process. This paper is intended to develop an innovative digital image-based reconstruction method for immediately generating the FE mesh models of heterogeneous materials by taking into account their actual microstructures. The reconstructed model is composed of four-node rectangular elements and eight-node rectangular hexahedral elements for 2D and 3D, respectively. Material properties of the elements are differentiated by the grayscale thresholds of the digital images to characterize the material components. It is demonstrated that the microstructural features with dimensions as small as the size of each image pixel can be accurately reconstructed.

2. Digital image acquisition and digitization

The real microstructures of heterogeneous materials are captured by X-ray tomography [14,15], which is an advanced technique for acquiring a stack of sectional images, with the advantage of rapidly acquiring accurate digital information of the internal microstructure in a non-destructive manner. The method is commonly applied using a relatively standard X-ray source and different material components are distinguished by their linear attenuation coefficients.

Fig. 1a illustrates a draft for obtaining the 3D serial images of heterogeneous materials. A cylindrical sample is cut and mounted for illustration. Then a left-handed coordinate system is built as shown in the figure. A representative rectangular surface region I_1 with width w and height h is selected to be the capture site of

the sectional image. The selection of the representative region is very important and meanwhile it is somewhat subjective. It is desirable to encompass several phase clusters in the representative region to allow entire clusters being reconstructed in the model; nevertheless, the amount of encompassed clusters should be restricted to maintain high image resolution and fast reconstruction speed. The digital image of the surface region is photographed with X-ray tomography. Then the scanning position of X-ray tomography is translated axially to a new position, which is parallel to the representative region without any displacements in x and y directions, to capture new sectional image. By repeating the above operation, a series of closely spaced slices are serially captured and a total number of D images are generated. In order to accurately characterize the microstructural features of the material, the distance $d_n (n = 1 \sim D - 1)$ between two successive sections I_n and I_{n+1} should be a value as small as possible to reach the size of each image pixel. Moreover, the selection of the total thickness of the D sections should assure that the reconstructed model encompasses several phase clusters in z direction.

Each acquired image is consisted of a rectangular array of image pixels, which can be specified by a pixel coordinate system as shown in Fig. 1b. The array size along i and j directions are respectively noted as W and H . Each image pixel is a square with size $s = w/W = h/H$. At each pixel, the image brightness is sensed and assigned with an integer value that is named as grayscale. For the mostly used 256 gray images, the grayscale has the integer interval from 0 to 255. As a result, the grayscale of pixel (i, j) in the pixel coordinate system can be expressed as a discrete function $g(i, j)$ and the 2D image can be noted as a matrix $[g(i, j)] (i = 1 \sim W, j = 1 \sim H)$. For a series of serial images, a left-handed k coordinate is added to the 2D pixel coordinate system to specify the serial numbers of images. In a similar way, discrete function $g(i, j, k)$ is used to express the grayscale of pixel (i, j, k) and the serial images are noted as a 3D array $\{g(i, j, k)\} (k = 1 \sim D)$.

3. Material component segmentation

The grayscale in the X-ray tomography image is mainly determined by the density of the material component. The higher the density, the more X-ray is absorbed by the material component, which results in higher grayscale value in the captured image.

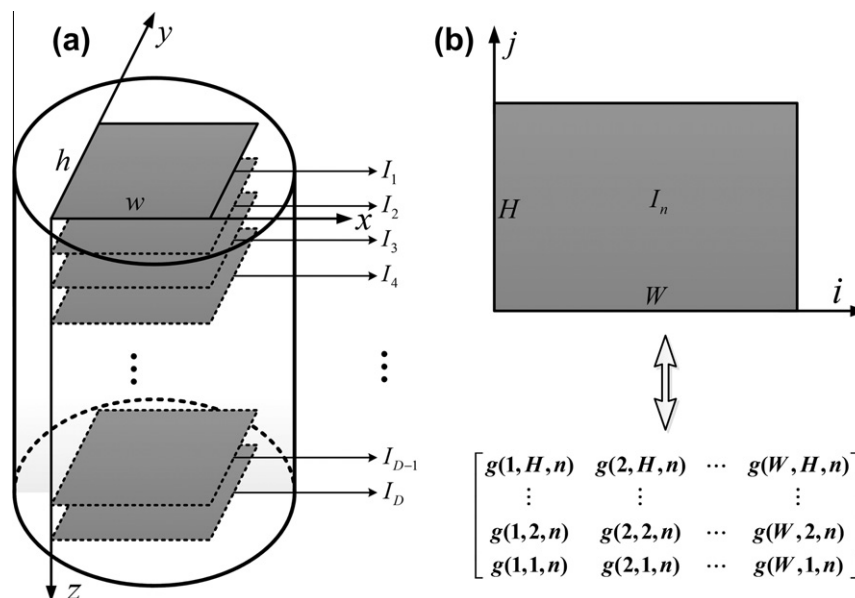


Fig. 1. Serial images acquisition and digitization: (a) Acquisition of 3D serial images. (b) Pixel coordinate system and image digitization.

According to this law, different material components can be segmented by the grayscale of the image. To segment the material components, the grayscale histogram $h(g)$ is introduced by counting the number of pixels with a certain grayscale:

$$h(g) = \text{count}_{1 \leq i \leq W, 1 \leq j \leq H} \{g(i, j) = g\} \quad (1)$$

Collection of these counts for all grayscales forms the histogram. This histogram function is, in general, a rough estimate of the grayscale density function.

Considering a typical two-phase heterogeneous material shown in Fig. 2a, which is a slice of original grayscale image of $\text{Al}_2\text{O}_3/(\text{W,Ti})\text{C}$ ceramic composite [16]. It is consisted of matrix material Al_2O_3 with density 3980 kg/m^3 and reinforced material $(\text{W,Ti})\text{C}$ with density 9490 kg/m^3 , thus the grayscale of Al_2O_3 (shown as black) is lower than that of $(\text{W,Ti})\text{C}$ (shown as white). The numbers of pixels along i and j directions are $W = 606$ and $H = 597$, while the actual sizes of the image are $w = 16.12 \mu\text{m}$ and $h = 15.88 \mu\text{m}$, thus the size of each pixel is consequently $s = 0.0266 \mu\text{m}$. Fig. 2b shows the histogram (vertical lines connected by solid line) of the $\text{Al}_2\text{O}_3/(\text{W,Ti})\text{C}$ ceramic composite. It illustrates that the grayscale of the two material components are mainly distributed around the wave crests 88 and 209, respectively. A wave trough at the grayscale 154 can be observed in Fig. 2b. The grayscale of the wave trough is the grayscale threshold, which is noted as T_1 , to segment the material components. The pixels with grayscale lower than the threshold T_1 represent Al_2O_3 while the others represent $(\text{W,Ti})\text{C}$.

The volume fraction of each phase can be determined by the cumulative distribution function $f(g)$, which is normalized by the amount of pixels in the image with the following formulation:

$$f(g) = \frac{1}{WH} \sum_{n \leq g} h(n) \quad (2)$$

The cumulative distribution function for $\text{Al}_2\text{O}_3/(\text{W,Ti})\text{C}$ ceramic composite is shown as a dash-dotted line in Fig. 2b. The volume fraction v_1 of matrix material Al_2O_3 is the value of $f(g)$ at threshold T_1 , that is to say, $v_1 = f(g)_{g=T_1} = f(154) = 53.55\%$.

The extension to multi-phase heterogeneous material with M phases, where $M > 2$, is straightforward. In this case, different phases in the material generally have different densities and thus different grayscale values in the X-ray tomography image. It is believed that thresholds $T_n (n = 1, 2, \dots, M - 1)$ can be obtained from the grayscale histogram and different material components can be differentiated by these threshold values. The pixels in the image with lower grayscales than T_1 belong to the phase that has the lowest density within the heterogeneous material and the volume fraction of this phase is $v_1 = f(g)_{g=T_1}$. While the pixels with grayscales in the interval $(T_1, T_2]$ belong to the phase that has the second lowest density and its volume fraction is $v_2 = f(g)_{g=T_2} - v_1$. The remaining phases and their volume fractions can be decided in a similar way.

As a validation of the proposed segmentation method, we compare the results of $\text{Al}_2\text{O}_3/(\text{W,Ti})\text{C}$ ceramic composite with the experimental data. The experiment reveals that the volume fraction v_1 of the matrix material Al_2O_3 is approximately 55.00%, therefore, the value determined by the X-ray tomography image is lower than the experimental data with a relative error of 2.64%. This discrepancy between these two volume fractions is mainly influenced by the inaccuracy of digital images, as the process of converting actual serial regions into digital images is very complicated and easily affected by external environment. Therefore, preliminary image processing such as image contrast enhancement and image noise reduction methods are needed to obtain a better result for the material microstructure reconstruction.

3.1. Image contrast enhancement

Image contrast enhancement can help to reproduce real material microstructure as it enhances the contrast between different inner material components. One particular method of interest, which is extensively used for enhancement of digital images, is the contrast limited adaptive histogram equalization (CLAHE) proposed by Pizer et al. [17] and realized by Zuiderveld [18]. Detailed mathematical description of CLAHE can be found in the excellent review paper given by Reza [19].

For the original image shown in Fig. 2a, it is processed by CLAHE and illustrated in Fig. 3a, which shows more obvious difference between the matrix and the reinforced material. In the enhancement process, the number of regions is selected to be 9 by equally dividing the image by 3 in each direction and the clip factor is appropriately selected to be 2 (refer to [19] for the meaning of the parameters).

The grayscale histogram and cumulative distribution function of the CLAHE processed image are depicted in Fig. 3b. The threshold value T_1 can be observed in the figure with a value $T_1 = 140$, and the volume fraction of the matrix material Al_2O_3 determined by the cumulative distribution function at the threshold is $v_1 = 54.92\%$. The relative error of the volume fraction to the experimental value is only 0.08%, which indicates that CLAHE contributes to the reconstruction of real microstructure.

3.2. Image noise reduction

Digital images are prone to be degraded by a variety of noises in the image acquisition and transmission process, which results in grayscale values do not reflect the real scenes [20]. In order to

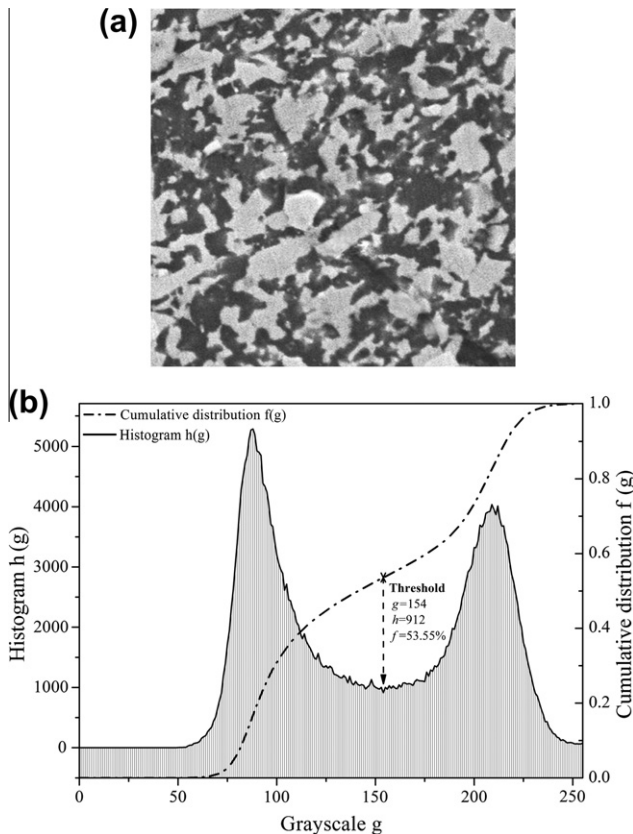


Fig. 2. An example of component segmentation: (a) A slice of X-ray tomography image for $\text{Al}_2\text{O}_3/(\text{W,Ti})\text{C}$ ceramic composite. (b) The grayscale histogram and cumulative distribution function for the image shown in (a).

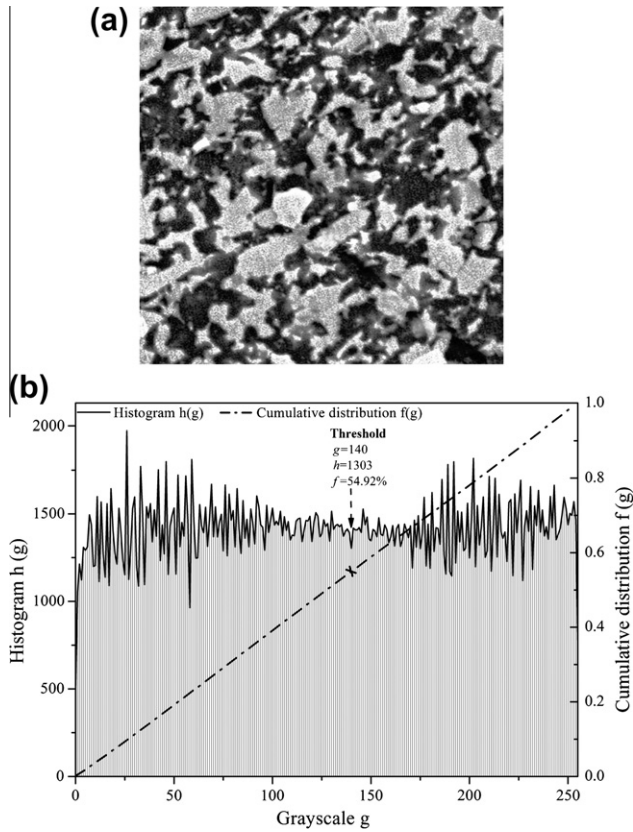


Fig. 3. Result of CLAHE processing: (a) CLAHE processed image. (b) The grayscale histogram and cumulative distribution function for the image shown in (a).

reduce the influence of noise on the microstructure reconstruction, noise reduction method is adopted here. The commonly used noise reduction methods include mean filters, order-statistics filters and adaptive filters. Among these methods, the best-known order-statistics median filter (MF) [21,22] is quite popular, because for certain types of random noise, it provides excellent noise reduction capabilities, with considerably less blurring the edges and other sharp details than any other methods.

By referencing to [20], the original image in Fig. 2a is processed by MF with a 3-by-3 neighborhood filtering window and the resultant image is shown in Fig. 4a. The histogram and cumulative distribution function of the processed image is illustrated in Fig. 4b. The threshold value observed in Fig. 4b is $T_1 = 154$, and the volume fraction of the matrix material Al_2O_3 is $v_1 = 53.63\%$, which is more accurate compared with that of the original image but is worse than that of the CLAHE processed image.

3.3. Combinational image processing

The above mentioned two image processing methods are individually performed on the image and each method helps to acquire the real microstructure of material. In order to investigate the effect of the combination of these methods, the original image shown in Fig. 2a is successively processed by CLAHE and MF, and by the reversed processes. The volume fractions determined by these two processed images are respectively 54.98% and 54.54%, with relative errors of 0.04% and 0.84%. By comparing the results with those of the original image and the images individually processed by CLAHE and MF, we can conclude that the image firstly processed by CLAHE and then by MF most accurately represents the real microstructure of the material. It is necessary to mention that the error of volume fraction estimated by X-ray tomography image is always there, no matter what kind of processing per-

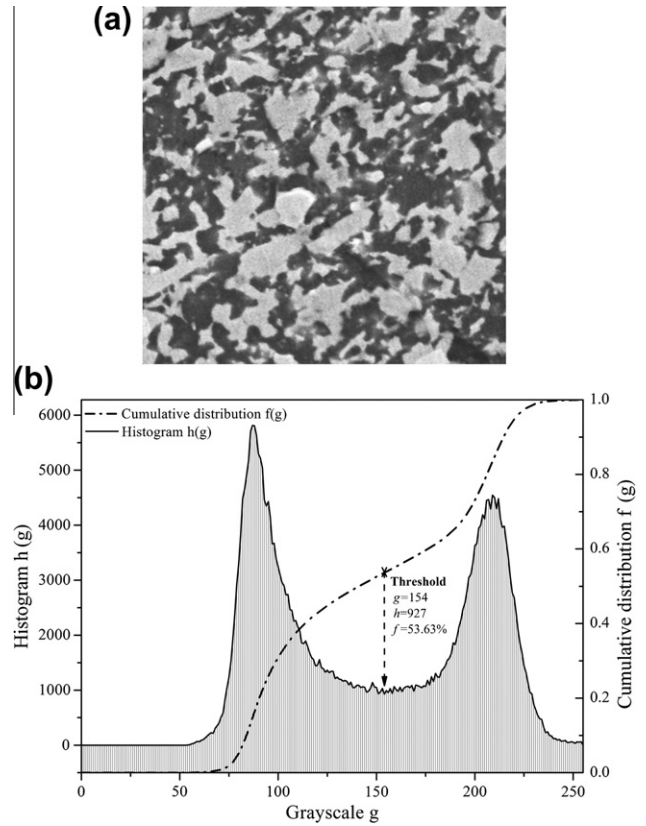


Fig. 4. Result of MF processing: (a) MF processed image. (b) The grayscale histogram and cumulative distribution function for the image shown in (a).

formed on the image. This is due to the resolution limit of the image, which cannot detect microstructures in the sample with dimensions less than the size of each pixel. High-resolution approaches can be used to acquire digital images of the material and it will clearly indicate that a higher-resolution image can detect more minor microstructures.

The image successively processed by CLAHE and MF is depicted in Fig. 5a for further study. The histogram and cumulative distribution function are shown in Fig. 5b, which demonstrates that the grayscale threshold of Al_2O_3 is 140. All the images used for reconstruction thereafter will be firstly processed by CLAHE and then by MF to most accurately take into account the microstructural features.

4. 2D FE mesh model reconstruction

In this section, the method of 2D FE mesh model reconstruction is introduced, which lays the foundation for 3D reconstruction. A monolayer of the serial images is firstly processed by CLAHE and MF. A 2D FE mesh model, whose elements form a one-to-one correspondence with the pixels of the image, is generated as shown in Fig. 6a. The model is consisted of four-node rectangular quadrilateral elements and the element size along x and y directions are equal to the actual size s of the pixels.

The identification numbers of the nodes and elements are assigned in the form as shown in Fig. 6b to provide a convenience for computing the coordinates of the nodes and determining the anticlockwise four-nodes of the elements. The coordinates of node n can be concisely computed by:

$$\begin{cases} x_n = (n-1)\%(W+1)s & n = 1, 2, \dots, (H+1)(W+1) \\ y_n = \lfloor \frac{n-1}{W+1} \rfloor s \end{cases} \quad (3)$$

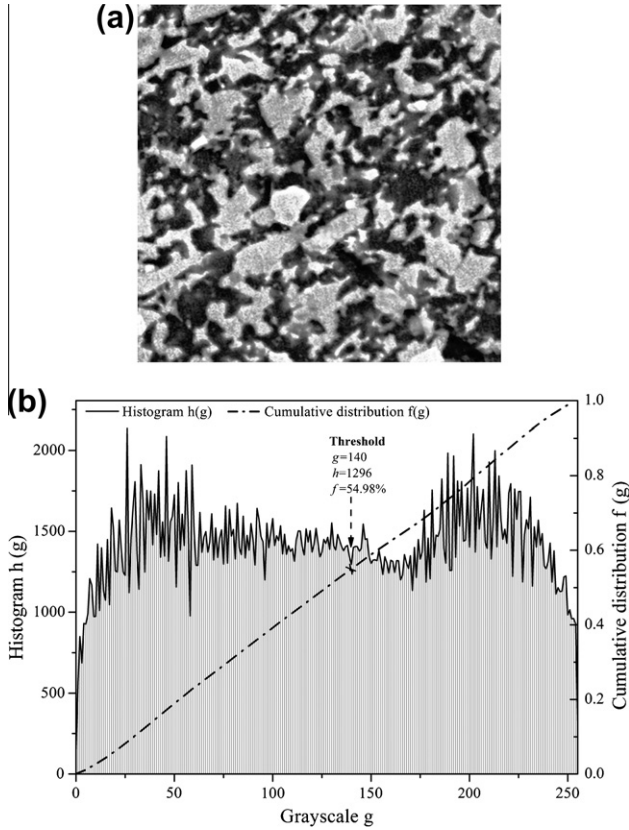


Fig. 5. Result of combinational processing: (a) Image successively processed by CLAHE and MF. (b) The grayscale histogram and cumulative distribution function for the image shown in (a).

where x_n and y_n are the coordinates of node n in x and y directions. In this paper, the operator “%” is modular arithmetic, which finds the remainder of division; while “ $\lfloor \cdot \rfloor$ ” is a round down operation to take the floor integer towards minus infinity. The anticlockwise four-nodes of the element n can be decided by the following formulations:

$$\begin{cases} N_n^1 = n + \lfloor \frac{n-1}{W} \rfloor \\ N_n^2 = N_n^1 + 1 \\ N_n^3 = N_n^1 + W + 2 \\ N_n^4 = N_n^1 + W + 1 \end{cases} \quad n = 1, 2, \dots, HW \quad (4)$$

where N_n^1, N_n^2, N_n^3 and N_n^4 are the anticlockwise four nodes of element n . The material property of element is determined by differentiating the grayscale of the mapping pixel using threshold value. In the FE mesh data file, the material property of element is characterized by its property identification number. The material property identification numbers of different material components in heterogeneous material are assumed to be natural numbers beginning with 1 and smaller numbers represent lower density components while greater numbers represent higher density ones. In this way, the material property p_n of element n can be decided by adopting the following criteria:

$$p_n = \begin{cases} 1, & g(i, j) \leq T_1 \\ r, & g(i, j) \in (T_{r-1}, T_r], \quad 1 < r < M \\ M, & g(i, j) > T_{M-1} \end{cases} \quad (5)$$

where i and j are decided by:

$$\begin{cases} i = 1 + (n - 1)\%W \\ j = 1 + \lfloor \frac{n-1}{W} \rfloor \end{cases} \quad (6)$$

By using the proposed 2D FE mesh reconstruction method, the $Al_2O_3/(W,Ti)C$ ceramic composite is reconstructed as shown in Fig. 7a based on the processed digital image in Fig. 5a. The most left-bottom one thirty-sixth part of the mesh model is shown in Fig. 7b to illustrate the microscopical details of the structure.

Compared with the original and processed images, the FE mesh model preserves most detailed microstructural information of the material. However, the number of elements in the mesh model is equal to that of pixels in the corresponding image, which is very enormous. With the resolution increased, the digital image will contain more pixels and the resultant FE mesh model will contain more elements, which is time-consuming for further FE analysis. As the pixels near image boundary are mostly affected by noise, we can trim the boundary pixels away from the perimeter to reduce the number of elements contained in the model.

4.1. Image trim

Considering the image shown in Fig. 5a, different amount of pixels are removed from the left, right, bottom and top of the image with almost equal increments to produce new images. The numbers of removed pixels are shown in Table 1. The grayscale thresholds, volume fractions of the matrix Al_2O_3 and relative errors for corresponding new images are also listed in Table 1, which shows that the relative errors of the investigated images are less than 2.79%. The amount of pixels trimmed can be determined subjectively by simultaneously considering the accuracy requirement and computation time. For instance, if the required accuracy is approximately not more than 1.00%, 28 surrounding pixels can be cut from the image in Fig. 5a to keep a relative error of 0.68%.

However, the more pixels trimmed, the less clusters or other microstructural features will be contained in the reconstructed model. This leads to the immediate challenge of balancing the

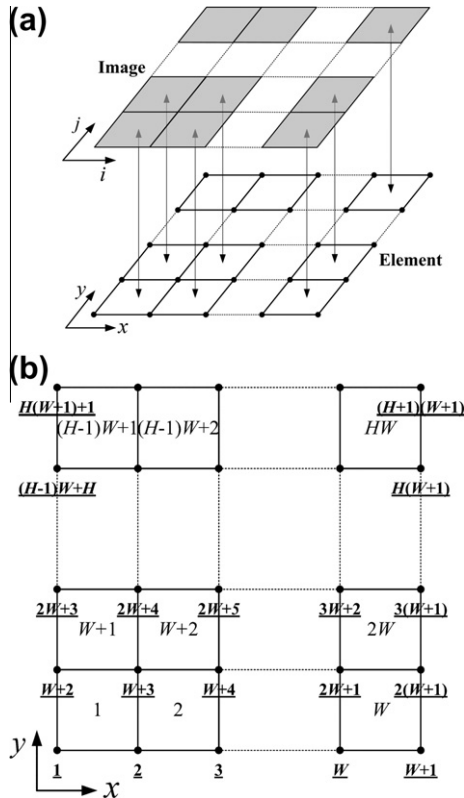


Fig. 6. 2D FE mesh model construction: (a) Mapping of 2D FE mesh model with image. (b) Numbering of nodes and elements.

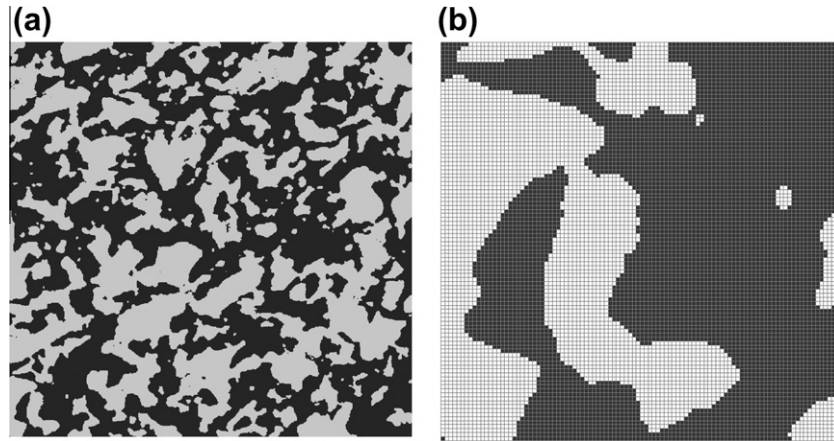


Fig. 7. An example of 2D FE mesh model reconstruction: (a) Reconstructed model for $\text{Al}_2\text{O}_3/(\text{W,Ti})\text{C}$ ceramic composite. (b) The detailed most left-bottom 1/36 part of the mesh model.

Table 1
Segmentation results for trimmed images.

Pixels removed				Threshold T_1	Volume fraction, v_1 (%)	Relative error, δ (%)
Left	Right	Bottom	Top			
0	0	0	0	140	54.98	0.043
8	8	9	8	140	55.11	0.21
18	18	19	18	139	54.73	0.49
28	28	29	28	139	54.63	0.68
38	38	39	38	139	54.42	1.06
48	48	49	48	139	54.06	1.71
58	58	59	58	139	53.89	2.02
68	68	69	68	139	53.93	1.94
78	78	79	78	139	54.00	1.82
88	88	89	88	139	53.96	1.89
98	98	99	98	139	54.28	1.31
108	108	109	108	139	54.30	1.27
118	118	119	118	139	54.32	1.24
128	128	129	128	139	54.16	1.54
138	138	139	138	139	53.46	2.79

image size and microstructural features included in the image, which can be investigated by merging the pixels.

4.2. Pixel merging

Pixel merging is realized by using the following formulation:

$$\hat{g}(i,j) = \left[\frac{1}{\alpha\beta} \sum_{r=(i-1)\alpha+1}^{i\alpha} \sum_{t=(j-1)\beta+1}^{j\beta} g(r,t) \right] \quad (7)$$

where $\hat{g}(i,j)$ is the pixel grayscale of the new image, α and β are the amount of pixels merged along i and j directions. If W and H cannot be divided exactly by α and β , respectively, the absent pixels outside the right and top boundaries are padded by replicating the values from the nearest border pixels. As the original grayscale values are averaged during the pixel merging process, the grayscale threshold for differentiating phases cannot be easily determined. It is reasonable to segment the image by adopting the threshold value determined by the raw image unprocessed by pixel merging and it is proved to very effective in the implementation.

As shown in Table 2, different amounts of pixels are merged for the image in Fig. 5a. The volume fractions of Al_2O_3 and relative errors for corresponding images are listed in the table. It is shown that the investigated image can be adjusted by merging less than 10 pixels in each direction with relative error of not more than

Table 2
Segmentation results for pixel merged images.

Pixels merged $\alpha = \beta$	Volume fraction, v_1 (%)	Relative error, δ (%)
1	54.97	0.043
2	55.12	0.22
3	55.06	0.11
4	54.97	0.056
5	54.92	0.14
6	55.10	0.18
7	55.19	0.34
8	54.88	0.22
9	55.27	0.49
10	56.07	1.94

1.94% to get smaller models while preserving the microstructural features of the material.

4.3. Illustrative reconstruction and model verification

A suitable ultimate image processed by image trim and pixel emerging that synthetically balanced the accuracy and computation time can be chosen by trial-and-error. Here, 28 surrounding pixels are trimmed from the image in Fig. 5a and the image is then processed by merging 5 pixels in each direction. The resultant image is formed with parameters of $W=110$, $H=108$, $T_1=140$, $v_1=54.81\%$ and $\delta=0.352\%$. The corresponding FE mesh model is illustrated in Fig. 8a.

To verify the applicability of the reconstructed FE mesh model, the homogenization method [23] is adopted to predict the macroscopic stiffness of $\text{Al}_2\text{O}_3/(\text{W,Ti})\text{C}$ ceramic composite. The elastic modulus and Poisson's ratio for matrix material Al_2O_3 and reinforced material $(\text{W,Ti})\text{C}$ are respectively:

$$\begin{aligned} E^{\text{matrix}} &= 400 \text{ GPa}, \quad \nu^{\text{matrix}} = 0.26, \quad E^{\text{reinforced}} = 570 \text{ GPa}, \\ \nu^{\text{reinforced}} &= 0.20 \end{aligned} \quad (8)$$

Based on the homogenization method, the elastic modulus and Poisson's ratio in x and y directions for the overall $\text{Al}_2\text{O}_3/(\text{W,Ti})\text{C}$ ceramic composite are predicted to be:

$$\begin{aligned} E_x^{\text{overall}} &= 474.42 \text{ GPa}, \quad E_y^{\text{overall}} = 474.26 \text{ GPa}, \\ \nu_x^{\text{overall}} &= 0.2296, \quad \nu_y^{\text{overall}} = 0.2311 \end{aligned} \quad (9)$$

Fig. 8b shows an accurate characteristic deformation of the FE model as a unit-cell, which indicates that the reconstructed FE mesh model is completely applicable to analyze the macroscopic properties of materials.

5. 3D FE mesh model reconstruction

The 3D microstructural model of heterogeneous material is reconstructed by stacking 2D serial images in z direction. CLAHE and MF are firstly applied to each serial image to accurately reflect the real sectional microstructures. As mentioned in Section 2, to present the actual microstructural features in z direction precisely, the distances between adjacent images should be almost the same size as the resolution of the 2D images, i.e., the following formula should be maintained:

$$E(d) + \sigma(d) \leq \xi s \quad (10)$$

where $E(d)$ and $\sigma(d)$ are the mathematical expectation and the standard deviation of the distances:

$$E(d) = \frac{1}{D} \sum_{n=1}^D d_n \quad (11)$$

$$\sigma(d) = \sqrt{\frac{1}{D} \sum_{n=1}^D (d_n - E(d))^2} \quad (12)$$

The coefficient ξ is circumstantially determined by the required accuracy of reconstruction and it is recommended to be in the interval of $1.0 \leq \xi \leq 2.0$. The vast majority of $d_n (n = 1, 2, \dots, D)$ is not greater than $E(d) + \sigma(d)$, thus Eq. (10) means that the serial

images can be directly used to reconstruct the 3D model if most of the distances are smaller than the upper bound ξs . On the contrary, if $E(d) + \sigma(d)$ exceeds the upper bound, the serial images should be interpolated to meet Eq. (10). New images between antecedent images will be generated and intermediate microstructural features be reproduced after interpolation. In the interpolation process, the amount of images interpolated between images I_n and I_{n+1} , and the adjacent distance of interpolated images are determined by:

$$D_n = \left\lfloor \frac{d_n}{\xi s} \right\rfloor \quad (13)$$

$$\hat{d}_n = \frac{d_n}{D_n} \quad (14)$$

The interpolated images and antecedent images are renumbered according to their coordinates in z direction. The grayscales of the interpolated images are calculated by:

$$g(i, j, k) = P(Z_k, g(i, j, n)), \quad k \in Ni, \quad n \in Na \quad (15)$$

where Ni and Na are number sets whose elements respectively point to interpolated and antecedent images; Z_k is the coordinate of the k th image along z direction; $P(Z, g)$ is a kind of approximation function interpolated by the points $(Z_n, g(i, j, n))$, $n \in Na$.

A 3D eight-node rectangular hexahedral FE mesh model is built to map with the serial images, as shown in Fig. 9a, each element layer maps to one image with a similar mapping method to two dimensional reconstruction.

The nodes and elements are numbered in the way as shown in Fig. 9b, which allows us to easily determine the coordinates of nodes and the eight-nodes of elements. The coordinates of node n is calculated by:

$$\begin{cases} x_n = \{(n-1)\%[(W+1)(H+1)]\}\%(W+1)s \\ y_n = \left\lfloor \frac{(n-1)\%[(W+1)(H+1)]}{W+1} \right\rfloor s \\ z_n = Z_r, \quad r = \left\lfloor \frac{n-1}{(W+1)(H+1)} \right\rfloor + 1 \end{cases} \quad n = 1, 2, \dots, (W+1)(H+1)(T+1) \quad (16)$$

where x_n , y_n and z_n are the coordinates of node n along x , y and z directions. The eight-nodes of element n can be concisely decided by the following formulations:

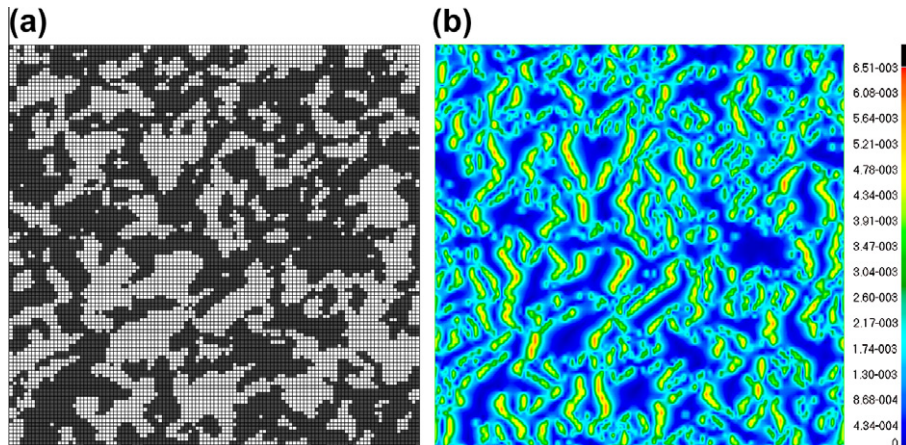


Fig. 8. Result of 2D FE mesh model reconstruction for $\text{Al}_2\text{O}_3/(\text{W,Ti})\text{C}$ ceramic composite: (a) Reconstructed model for $\text{Al}_2\text{O}_3/(\text{W,Ti})\text{C}$ after applying image trim and pixel merging. (b) Characteristic deformation shown on undeformed model.

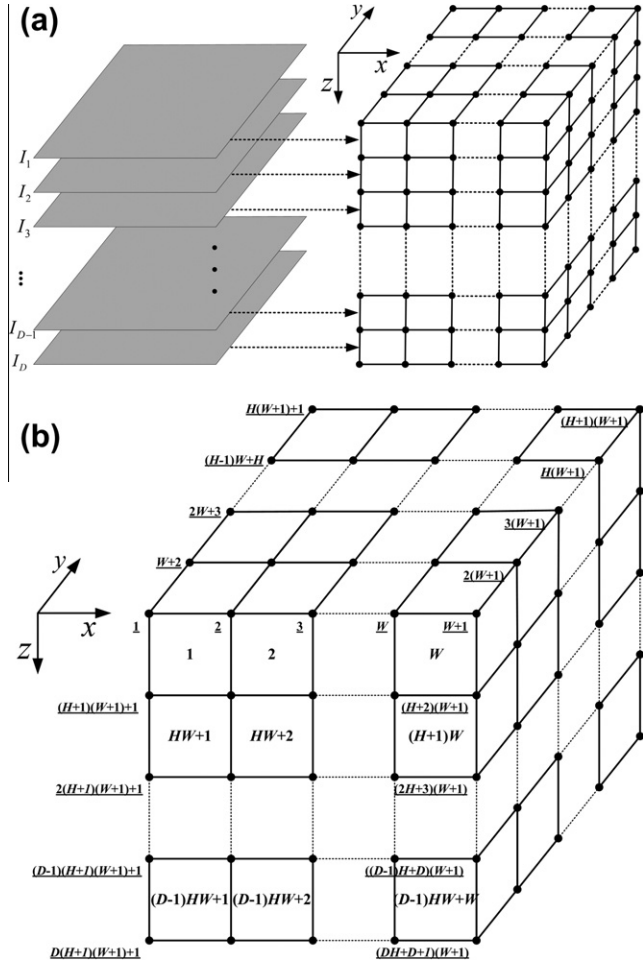


Fig. 9. 3D FE mesh model construction: (a) Mapping of 3D FE mesh model with serial images. (b) Numbering of nodes and elements.

$$\begin{cases} N_n^1 = n + \lfloor \frac{n-1}{W} \rfloor + \lfloor \frac{n-1}{WH} \rfloor (W+1) \\ N_n^2 = N_n^1 + 1 \\ N_n^3 = N_n^1 + W + 2 \\ N_n^4 = N_n^1 + W + 1 \\ N_n^r = N_n^{r-4} + (W+1)(H+1), \quad r = 5, 6, 7, 8 \end{cases} \quad n = 1, 2, \dots, WHT \quad (17)$$

where N_n^r ($r = 1, 2, \dots, 8$) are the eight nodes of element n . The same procedure in 2D reconstruction can be applied to decide the material property p_n of element n by the grayscale of corresponding image pixel and the thresholds with a similar formulation:

$$p_n = \begin{cases} 1, & g(i, j, k) \leq T_1 \\ r, & g(i, j, k) \in (T_{r-1}, T_r], \quad 1 < r < M \\ M, & g(i, j, k) > T_{M-1} \end{cases} \quad (18)$$

The pixel coordinate (i, j, k) of element n is determined by:

$$\begin{cases} i = 1 + (n-1)\%W \\ j = 1 + \lfloor \frac{(n-1)\%(HW)}{W} \rfloor \\ k = 1 + \lfloor \frac{n-1}{HW} \rfloor \end{cases} \quad (19)$$

Considering the aforementioned $\text{Al}_2\text{O}_3/(\text{W,Ti})\text{C}$ ceramic composite, eleven serial images are captured by X-ray tomography as shown in Fig. 10a. The pixel width and height of these images

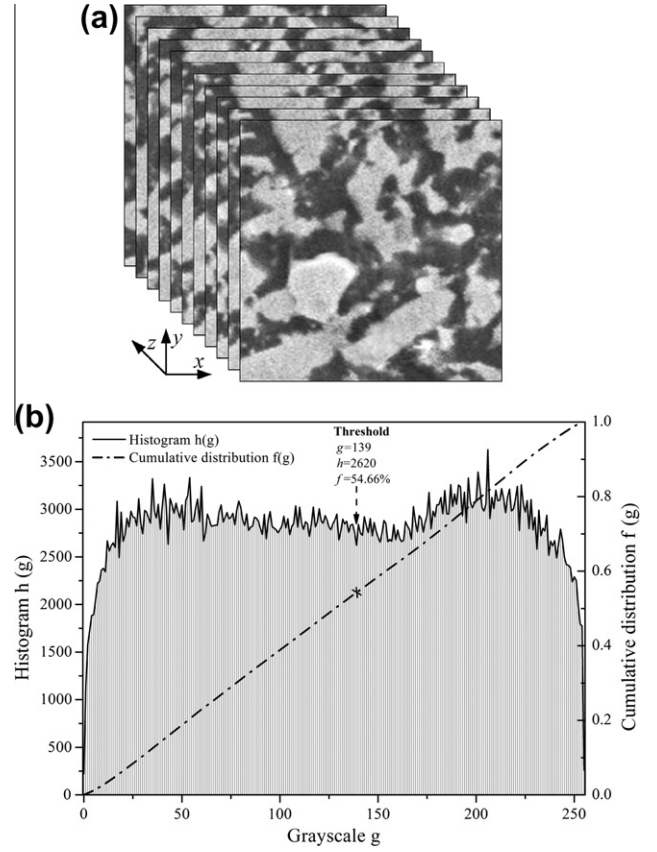


Fig. 10. An example of 3D serial images segmentation: (a) Eleven serial images for $\text{Al}_2\text{O}_3/(\text{W,Ti})\text{C}$ ceramic composite. (b) The grayscale histogram and cumulative distribution function for the image shown in (a).

are $W = H = 256$, while the real sizes are $w = h = 6.8096 \mu\text{m}$. All the distances between adjacent images are $d_n = 0.158 \mu\text{m}$ ($n = 1, 2, \dots, D-1$).

The serial images are successively processed by CLAHE and MF to accurately reflect the real microstructure. The histogram and

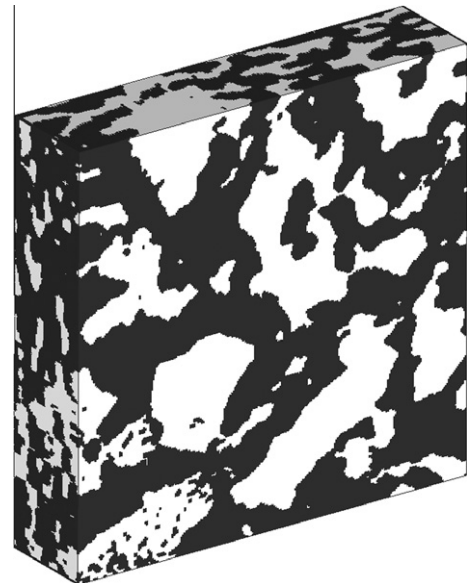


Fig. 11. Result of 3D FE mesh model reconstruction for $\text{Al}_2\text{O}_3/(\text{W,Ti})\text{C}$ ceramic composite.

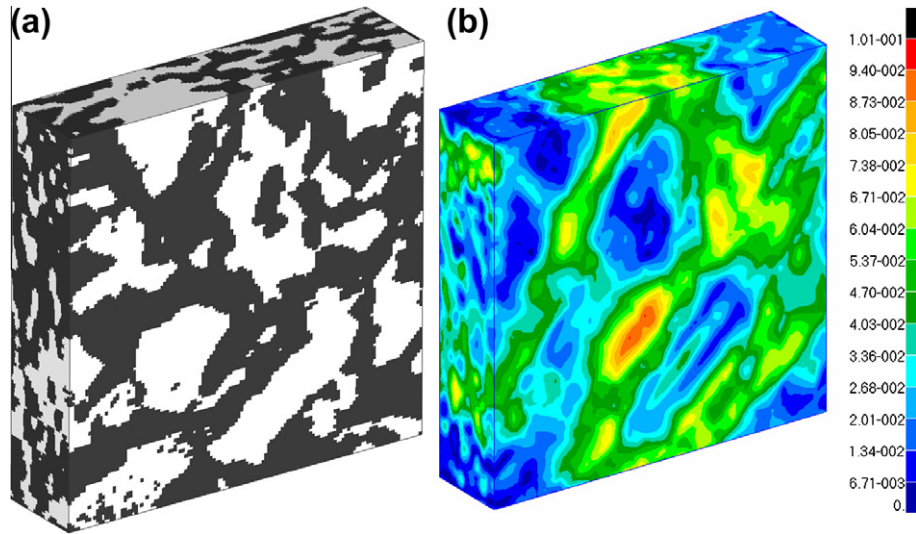


Fig. 12. 3D FE mesh model for $\text{Al}_2\text{O}_3/(\text{W,Ti})\text{C}$ ceramic composite: (a) Reconstructed 3D model for $\text{Al}_2\text{O}_3/(\text{W,Ti})\text{C}$ after applying pixel merging. (b) Characteristic deformation shown on undeformed model.

cumulative distribution function of these images are illustrated in Fig. 10b, which indicates that the grayscale threshold is 139 and the corresponding volume fraction of Al_2O_3 is 54.66% with a relative error of 0.62%.

As $E(d) + \sigma(d)$ exceeds the upper bound $\zeta s = 0.0266 \mu\text{m}$ (ζ is selected to be 1.0), the natural cubic spline interpolation is applied to the serial images. After the pixel interpolation, there are 61 images in the new series and the updated distance between adjacent images is $0.0263 \mu\text{m}$, which is small enough to reconstruct microstructural features. As shown in Fig. 11, the 3D FE mesh model is reconstructed by adopting the grayscale threshold of 139. Note that the threshold is decided by the CLAHE and MF processed images rather than the interpolated images. The volume fraction ν_1 of the reconstructed model is 55.21%, which is 0.38% greater than the experimental value.

The reconstructed 3D models usually contain a great amount of elements, which results in time-consuming for further FE analysis. Image trim and pixel merging proposed in Section 4 can be applied to the serial images by judging and weighing the reconstruction accuracy and computation time. Note that the same processes should be exactly applied to each image to keep the microstructure alignment along z direction and maintain equal numbers of pixels along x and y directions. For the serial images in Fig. 10a, 2 pixels are merged in each direction and the resultant 3D FE mesh model is shown in Fig. 12a with a relative error of 0.49%.

The applicability of the reconstructed 3D FE mesh model is also verified by predicting the macroscopic stiffness of $\text{Al}_2\text{O}_3/(\text{W,Ti})\text{C}$ ceramic composite based on the homogenization method. The microscopic mechanical properties of the material components have been provided in Section 4. The elastic modulus and Poisson' ratio in various directions for the overall $\text{Al}_2\text{O}_3/(\text{W,Ti})\text{C}$ ceramic composite are predicted as follows:

$$E_x^{\text{overall}} = 472.04 \text{ GPa}, \quad E_y^{\text{overall}} = 471.87 \text{ GPa}, \quad E_z^{\text{overall}} = 469.36 \text{ GPa} \quad (20)$$

$$\nu_x^{\text{overall}} = 0.235, \quad \nu_y^{\text{overall}} = 0.233, \quad \nu_z^{\text{overall}} = 0.232 \quad (21)$$

It is easy to see that the properties in the xy plane are almost the same as those predicted by the 2D model. The characteristic deformation of the FE mesh model is shown in Fig. 12b. The figure illustrates the real microstructural deformation form of typical

heterogeneous material. The reconstructed models can be used to accurately predict other macroscopic properties of heterogeneous materials, which will be presented in further studies.

6. Summary

This paper presents a novel FE mesh model reconstruction method based on the X-ray tomography image for heterogeneous materials by directly taking their real microstructures into account. In this method, serial images are captured by X-ray tomography to reflect the microstructural features, and the images are digitized to grayscale matrices or 3D array. The grayscale histogram is introduced to decide thresholds for segmenting the images into different material components. The volume fractions of the material components are determined by the grayscale cumulative distribution function. By mapping with the segmented serial images, 2D and 3D FE mesh models with rectangular quadrilateral and hexahedral elements are reconstructed. Besides, the image contrast enhancement, noise reduction and pixel interpolation methods are applied to the images to accurately reflect the actual microstructures, while image trim and pixel merging are proposed to reduce the elements contained in the reconstructed model.

The proposed method is implemented by using the C++ programming language and Windows GDI platform. The developed program package outputs the FE mesh models in the neutral file format used in MSC.Nastran. Using $\text{Al}_2\text{O}_3/(\text{W,Ti})\text{C}$ ceramic composite as an example, the paper has shown that the proposed method can be used to efficiently reconstruct the microstructures with high accuracy.

The method overcomes the shortcomings of traditional modeling approaches by reconstructing the FE mesh models of heterogeneous materials directly. The reconstructed models accurately reflect the microstructural features of materials and they could be immediately used for FE analysis to predict the macroscopic properties, and this will be very helpful to design and optimize the high performance heterogeneous materials.

Acknowledgements

The authors are grateful to the Ministry of Science and Technology of China for its support through the 973 Program

(2009CB724402) and the National Natural Science Foundation of China (Grant No. 11021202).

References

- [1] S. Torquato, *Annu. Rev. Mater. Res.* 32 (2002) 77–111.
- [2] L.L. Mishnaevsky, *Mater. Sci. Eng. A* 407 (2005) 11–23.
- [3] L.L. Mishnaevsky, S. Schmauder, *Appl. Mech. Rev.* 54 (2001) 49–67.
- [4] A.A. Gusev, *J. Mech. Phys. Solids* 45 (1997) 1449–1459.
- [5] A. Eckschlager, W. Han, H.J. Bohm, *Comp. Mater. Sci.* 25 (2002) 85–91.
- [6] D.A. Jerram, M.D. Higgins, *Elements* 3 (2007) 239–245.
- [7] A. Ayyar, N. Chawla, *J. Mater. Sci.* 42 (2007) 9125–9129.
- [8] N. Chawla, R.S. Sidhu, V.V. Ganesh, *Acta Mater.* 54 (2006) 1541–1548.
- [9] D. Jianjun, L. Jianrong, Q. Aike, L. Youjun, in: *3rd Int. Conf. Bioinf. Biomed. Eng.* (2009) 1–4.
- [10] M.D. Uchic, L. Holzer, B.J. Inkson, E.L. Principe, P. Munroe, *MRS Bull.* 32 (2007) 408–416.
- [11] A. Klemm, H.P. Muller, R. Kimmich, *Phys. Rev. E* 55 (1997) 4413–4422.
- [12] C.L.Y. Yeong, S. Torquato, *Phys. Rev. E* 58 (1998) 224–233.
- [13] C.L.Y. Yeong, S. Torquato, *Phys. Rev. E* 57 (1998) 495–506.
- [14] J. Liu, K. Regenauer-Lieb, *Phys. Rev. E* 83 (2011) 016106.
- [15] Z.T. Karpyn, M. Piri, *Phys. Rev. E* 76 (2007) 016315.
- [16] Y.H. Zhou, X. Ai, J. Zhao, F.Z. Yang, X. Qiang, *J. Synth. Cryst.* 37 (2008) 809–813.
- [17] S.M. Pizer, E.P. Amburn, J.D. Austin, R. Cromartie, A. Geselowitz, T. Greer, B.T.H. Romeny, J.B. Zimmerman, K. Zuiderveld, *Comput. Vis., Graphics, Image Process.* 39 (1987) 355–368.
- [18] K. Zuiderveld, Contrast limited adaptive histogram equalization, in: P.S. Heckbert (Ed.), *Graphics Gems*, vol. IV, Academic Press Professional Inc., Cambridge, MA, 1994, pp. 474–485.
- [19] A.M. Reza, *J. VLSI Sig. Proc. Syst.* 38 (2004) 35–44.
- [20] R.C. Gonzalez, R.E. Woods, *Digital Image Processing*, second ed., Prentice Hall, New Jersey, 2001.
- [21] B.R. Frieden, *J. Opt. Soc. Am.* 66 (1976) 280–283.
- [22] T. Huang, G. Yang, G. Tang, *Signal Process.* 27 (1979) 13–18.
- [23] J.M. Guedes, N. Kikuchi, *Comput. Meth. Appl. Mech. Eng.* 83 (1990) 143–198.